Chemical Science

ROYAL SOCIETY OF CHEMISTRY

EDGE ARTICLE

View Article Online
View Journal

Cite this: DOI: 10.1039/d6sc03818b

All publication charges for this article have been paid for by the Royal Society of Chemistry

Role of the Fe–$FeCl_2$ contact interface in promoting redox reversibility and electrochemical kinetics in Fe/$FeCl_2$–graphite molten salt batteries

Wenlong Zhang and Xiaohui Ning *

The Fe/$FeCl_2$–graphite battery is an intermediate-temperature molten salt electrochemical system. It employs the solid Fe/Fe^{2+} redox couple as the negative electrode and a graphite positive electrode based on the intercalation/de-intercalation of $AlCl^-_4$, offering high safety, low material cost and a moderate operating temperature range of 110–150 °C. However, the poor electronic conductivity and high nucleation barrier of the $FeCl_2$ material result in limited electrochemical reversibility and reaction kinetics. Here, we demonstrate that the Fe–$FeCl_2$ contact interface effectively enhances the redox reversibility and electrode kinetics by providing favorable sites for Fe^0 nucleation and improving electronic conductivity. The prepared Fe–$FeCl_2$–CR electrode delivers a low voltage hysteresis of 0.09 V and exhibits excellent electrochemical reversibility in the Fe/$FeCl_2$–graphite molten salt battery, achieving a specific capacity of 162.6 mAh g^{-1} at 3 mA cm^{-2} and retaining 93% of its capacity after 200 cycles. Compared with the pure $FeCl_2$ electrode, the Fe–$FeCl_2$–CR electrode shows lower direct-current pulse resistance and negligible nucleation overpotential, which are primarily attributed to the Fe-philic nucleation interface. This mechanism is further confirmed by density functional theory (DFT) calculations, revealing that the (110) crystal plane of nano-Fe possesses the highest binding energy (−55.94 eV) during charging, thereby serving as the potential dominant interface for Fe^0 nucleation. Additional self-discharge and capacity expansion tests further confirm the electrochemical reaction stability of the Fe–$FeCl_2$–CR electrode in Fe/$FeCl_2$–graphite molten salt batteries.

Received 7th May 2026
Accepted 4th June 2026

DOI: 10.1039/d6sc03818b

rsc.li/chemical-science

1. Introduction

The global transition toward renewable and sustainable energy has accelerated the need for advanced large-scale electrical energy storage technologies to support the integration of intermittent clean energy sources. Driven by market demands, the evolution of rechargeable battery-based large-scale storage systems imposes increasingly stringent requirements on cost-effectiveness, safety, and cycle life.[1] There is an urgent need to develop highly reversible electrochemical systems with intrinsically safe electrode and electrolyte materials. Molten salt batteries utilizing inorganic ionic liquids offer distinct advantages in terms of electrode reaction kinetics, electrolyte safety, and ionic conductivity.[2] For instance, novel low melting point molten salt electrode materials (NMPV, SMS-FeX_3, QASs-NMP, *etc.*) formed by the coordination complexation of metallic/non-metallic ion (Fe^{3+}, V^{3+}, Co^{2+}, quaternary ammonium salts, *etc.*) with the lone pair electrons of *N*-methyl pyrrolidone (NMP) were found to exhibit excellent electronic conductivity and electrochemical activity, and demonstrate high lithium-ion storage capacity and stable electrode reactions.[3–6] Owing to their unique three-layer liquid electrode/electrolyte structure, the rapid electron/ion exchange at the liquid metal/ionic liquid interface endows liquid metal batteries with excellent power density, enabling operation at high current densities of up to 1250 mA cm^{-2}.[7]

Leveraging the stable chemical properties of Na^+-conducting solid electrolytes (*e.g.*, β-Al_2O_3) and the high electrode potential of metal chloride electrodes (*e.g.* $NiCl_2$, $FeCl_2$, and $ZnCl_2$), sodium-metal chloride batteries demonstrate high discharge voltage and good electrochemical activity within a medium-temperature range of 150–200 °C.[8,9] Furthermore, the intercalation/de-intercalation of $AlCl^-_4$ anions into graphite interlayers has been shown to exhibit outstanding electrochemical reversibility in aluminum-ion batteries, both in room-temperature ionic liquid electrolytes and inorganic molten salt electrolytes. For example, a 3D graphite foam positive electrode showed nearly negligible capacity decay after 7500 cycles at a high current density of 4 A g^{-1} in an $AlCl_3$/[EMIm]Cl ionic liquid electrolyte at room temperature.[10] Meanwhile, commercial graphite paper used as the positive electrode in aluminum-ion batteries has also demonstrated a high specific capacity of 114.9 mAh g^{-1} after 1500 cycles (at 0.2 A g^{-1}) in a quaternary low-melting-point molten salt electrolyte ($AlCl_3$–NaCl–LiCl–

Center for Alloy Innovation and Design (CAID), State Key Laboratory for Mechanical Behavior of Materials, Xi'an Jiaotong University, Xi'an, Shaanxi 710049, P. R. China. E-mail: xiaohuining@mail.xjtu.edu.cn

KCl). Notably, the cost of such inorganic molten salt electrolytes is approximately one-sixth that of organic ionic liquid electrolytes (*e.g.*, $AlCl_3$/[EMIm]Cl with a molar ratio of 1.3).[11]

Focusing on lower operating temperatures and high-abundance electrode/electrolyte materials, a novel Fe/$FeCl_2$–graphite molten salt battery was first proposed in 2019 by Ning *et al.*, based on a $NaAlCl_4$ molten salt electrolyte at 170 °C. In this system, the positive and negative electrodes inherit the reaction mechanisms of the graphite electrode from aluminum ion batteries and the metal chloride electrode from sodium–metal chloride batteries, respectively.[12,13] During charging, the graphite positive electrode primarily undergoes the intercalation of AlCl-4 ions to form graphite intercalation compounds (GICs), while a reduction reaction occurs at the $FeCl_2$ negative electrode, generating solid metallic iron (Fe) and sodium chloride (NaCl). When paired with the Fe/$FeCl_2$ foam metal negative electrode, the graphite positive electrode delivered a specific capacity of approximately 104 mAh g^{-1}, with 85% capacity retention after 10 000 cycles. Unlike the liquid deposition of Fe^{2+} in iron-metal batteries or the solid-state oxidation of Fe in Na–$FeCl_2$ molten salt batteries, the initial active material in the fully discharged Fe/$FeCl_2$–graphite battery is solely $FeCl_2$.[14] The poor electronic conductivity and high nucleation energy barrier for the $FeCl_2$ → Fe conversion are the main factors limiting the development of $FeCl_2$ negative electrodes with high electrochemical reversibility. Previous studies have shown that fabricating $FeCl_2$ active material at an iron matrix interface can not only improve the electrical conductivity but also provide an Fe-philic nucleation interface for the reduction of $FeCl_2$. For instance, Ning *et al.* investigated the electrochemical properties of $FeCl_2$/Fe negative electrodes synthesized *via* HCl gas-phase chemical chlorination and galvanostatic/potentiostatic electrochemical chlorination within an iron foam matrix. The Fe/$FeCl_2$–EAE-1.4 V electrode, prepared by galvanostatic electrochemical chlorination, exhibited lower electrochemical polarization and a higher areal capacity (0.72 mAh cm^{-2} at 5.0 mA cm^{-2} after 7000 cycles) compared to the sample prepared by HCl gas-phase chlorination in the Fe/$FeCl_2$–graphite molten salt battery.[15] Similarly, Wu *et al.* studied the Fe^{2+}/Fe^0 redox couple in an $AlCl_3$/[EMIm]Cl ionic liquid electrolyte using an iron foil positive electrode and an aluminum negative electrode.[16] Their results indicated that at appropriate current densities (0.2 mA cm^{-2}), a 304-type austenitic stainless-steel foil (50 μm thick) used as an Fe nucleation interface in an Al–Fe battery achieved a coulombic efficiency of 99% and an areal capacity of 0.74 mAh cm^{-2}. However, whether in foam metal or foil electrodes, Fe atoms within the bulk material have limited participation in surface electrode reactions, leading to low active material utilization and constrained electrode energy density. Therefore, designing $FeCl_2$ negative electrode preparation strategies that maximize the Fe–$FeCl_2$ contact interface is an effective approach to developing high-energy-density Fe/$FeCl_2$–graphite molten salt battery.

In this work, we designed the Fe–$FeCl_2$ contact interface *via* a direct dry-powder calendering process. A substantial Fe–$FeCl_2$ contact interface was achieved by ball milling nano-Fe powder with $FeCl_2$ powder, which effectively enhanced the redox electrochemical activity of the Fe/$FeCl_2$ negative electrode. The nano-Fe powder not only serves as an Fe-philic nucleation interface to guide the distribution of the reduction product (Fe^0) but also significantly improves the electronic conductivity of the composite electrode. $FeCl_2$ was used as the starting active material to meet the assembly requirements of the fully discharged initial state. First, we investigated the effect of nano-Fe powder addition on electrochemical performance at different active material ratios in Fe/$FeCl_2$–graphite full cells. The results show that the Fe–$FeCl_2$–CR-60 electrode delivered a specific capacity of 162.6 mAh g^{-1} at 3 mA cm^{-2} and retained 93% of its capacity after 200 cycles, with active material utilization increasing to 27.15%. Second, we examined the electrochemical interface characteristics of electrodes containing nano-Fe powder using Al–Fe half-cells and a three-electrode system. Compared to the pure $FeCl_2$ electrode, the Fe–$FeCl_2$–CR-60 electrode exhibited a low redox overpotential of 90 mV and a DC pulse resistance of 1.74 Ω, confirming high electrochemical reversibility and a low nucleation energy barrier at the Fe–$FeCl_2$ interface. Finally, reaction mechanism analysis of the Fe–$FeCl_2$–CR-60 electrode indicated that the full-cell charging process corresponds to the conversion of $FeCl_2$ to Fe^0 and crystalline NaCl, and the surface of the added nano-Fe powder gradually transforms into an active interface during cycling. Furthermore, Fe/$FeCl_2$–graphite full cells assembled with Fe–$FeCl_2$–CR-60 negative electrodes exhibited low self-discharge (retaining the initial discharge capacity of 196.7 mAh g^{-1} after 168 hours of cooling storage) and good scalability (electrode area = 11.3 cm^2; initial electrode capacity = 13 mAh). This Fe–$FeCl_2$ contact interface provides valuable insights for the future large-scale development of intermediate-temperature Fe/$FeCl_2$–graphite molten salt batteries.

2. Materials and methods

2.1 Preparation of molten salt electrolyte

The preparation of the molten salt electrolyte primarily involves dehydration heating and pre-melting under an Ar atmosphere. NaCl (99.5%, Aladdin), $AlCl_3$ (99%, Aladdin), and LiCl (99%, Aladdin) are first subjected to preliminary dehydration treatment in a resistance furnace. Given its low melting point (194 °C) and sublimation temperature (183 °C), $AlCl_3$ is pretreated at 80 °C for 12 h. The remaining salts, LiCl and NaCl, are heated separately at 80 °C and 250 °C for 12 h, respectively. After dehydration, the salts are mixed in the molar ratio of $AlCl_3$: LiCl : NaCl = 2 : 1 : 1. The resulting ternary electrolyte has a melting point of approximately 105 °C; therefore, the mixed salts are pre-melted at 200 °C for 12 h and then at 150 °C for 24 h. During this stage, high-purity aluminum strips are added to remove impurities from the melt until the electrolyte becomes transparent. After the pre-melting process, the molten salt electrolyte is allowed to cool naturally, and the resulting solid white blocks are ground and collected.

2.2 Preparation of Fe–$FeCl_2$–CR electrodes

The preparation of Fe–$FeCl_2$–CR electrodes is carried out by dry powder roll-to-rolled calendering. Firstly, anhydrous $FeCl_2$

(99.5%, Aladdin) was ball milled at 500 rpm for 6 hours in an Ar atmosphere. Secondly, the obtained anhydrous $FeCl_2$ was uniformly mixed with acetylene black (AB, 99.9%, Alfa Aesar), polytetrafluoroethylene (PTEF, Aladdin) and nano Fe powder (50 nm, 99.9%, Macklin) in a mass ratio of $FeCl_2$ + Fe : AB : PTEF = 40 : 30 : 30 wt%. The mixed materials were rolled repeatedly by using an electric roller machine (MSK-2150, KEJING STAR Technology Co., Ltd) until the thickness of electrode material was about 10 μm, and the active substance loading was 6–8 mg cm^{-2}. Due to the electrochemical activity of nano-Fe powder, all electrode specific capacity calculations are based on the total mass of Fe + $FeCl_2$. In all three-electrode tests, a metal molybdenum (Mo) mesh was used as the electrode current collector for fixation. Finally, the calendered electrode was cut into discs with a diameter of 10 mm. All obtained electrodes were kept at 250 °C for 12 hours in an Ar atmosphere for cross-linking and moisture removal. To investigate the electrochemical reaction behavior of nano-Fe and $FeCl_2$, electrodes with different contents and material ratios (0, 20, 40, 60, 80 and 100 wt%) were prepared and named Fe-CR, Fe-$FeCl_2$-CR-*xx* and $FeCl_2$-CR according to the same steps.

2.3 Electrochemical measurements

The structure of the testing batteries is based on our previous research literature.[17] Firstly, the pre-melted electrolyte is placed in a quartz crucible and remelted at 150 °C. An appropriate molten salt electrolyte is added to the internal cavities of the positive and negative electrodes, in which the molten electrolyte acts as a separator to prevent short circuiting. Due to its low viscosity and excellent fluidity, the electrolyte fully wets the surfaces of the positive and negative electrodes. After the molten electrolyte solidifies, molybdenum foil current collectors (50 μm, 99.99%) are placed in contact with the graphite positive electrode (0.1 mm, Shandong Huatai graphite) and the calendered Fe/$FeCl_2$ negative electrode respectively. Finally, the stainless-steel shells are placed contact with the molybdenum foil and fixed using nut clamps. All the above operations are carried out in a glove box filled with Ar, under O_2 < 1.0 ppm and H_2O < 1.0 ppm. The assembled batteries are tested at 130 °C in air. The galvanostatic charging and discharging tests are mainly conducted by using a Neware battery tester (CT-4008T-5V10MA), while the tests of capacity expanded batteries and pulse resistance are performed by applying an Arbin BT2000 instrument. For all three-electrode tests, aluminum foil (100 μm, 99.999%) is used as the reference electrode and counter electrode. The corresponding cyclic voltammetry is carried out by using an electrochemical workstation (Autolab-PGSTAT204, Metrohm).

2.4 Material characterization

X-ray powder diffraction (XRD, X'Pert PRO, PANalytical B.V.) is employed to detect the composition and structural changes of electrode materials. Scanning electron microscopy (SEM, SU6600, Japan) and energy-dispersive X-ray spectroscopy (EDX) are utilized to observe the morphology and surface elements of the electrode materials, with an accelerating voltage of 15 kV and a working distance of 10 mm. To explore the variation of the graphite carbon atom vibration state before and after the charging process, Raman spectroscopy (DXR3xi, Thermo Fisher Scientific) is adopted to detect the graphite material in the initial state and the fully charged state, with a laser wavelength of 532 nm and a power of 3.2%.

2.5 Calculation method

Density functional theory as implemented in the Vienna *Ab initio* Simulation Package (VASP)[18,19] is employed to optimize geometry structures. The exchange–correlation interactions are described by the generalized gradient approximation (GGA) in the form of the Perdew–Burke–Ernzerhof functional (PBE).[20] We have chosen the projected augmented wave (PAW) potentials[21,22] to describe the ionic cores and take valence electrons into account using a plane wave basis set with a kinetic energy cutoff of 450 eV. The electronic energy is considered self-consistent when the energy change is smaller than 10^{-5} eV. A geometry optimization is considered convergent when the force change is smaller than 0.04 eV $Å^{-1}$. The vacuum spacing in the direction perpendicular to the plane of the structure is 15 Å. The van der Waals interactions are considered by using the Grimme (DFT + D3) method.[23] The Brillouin-zone integration is sampled with a Monkhorst–Pack mesh of 2 × 2 × 1 in the structural relaxation calculations. The binding energy is presented by the formula:

$$E_{bind} = E_{substrate+mol} - E_{substrate} + E_{mol}$$

where $E_{substrate+mol}$ is the total energy of the substrate with adsorbed molecules, $E_{substrate}$ is the energy of the clean surface of the slab model, E_{mol} is the energy of a single molecule in the gas phase.

3. Results and discussion

In the Fe/$FeCl_2$–graphite molten salt battery, the electrochemical reversibility and energy density of the Fe^{2+}/Fe^0 redox couple are limited by the accessible Fe/$FeCl_2$ interface at the electrolyte. Electrode preparation methods based on the chemical or electrochemical surface oxidation of the Fe matrix struggle to ensure sufficient electrode reaction sites within the Fe bulk. Moreover, the aggressive ionic environment of molten salt electrolytes compromises the chemical stability of electrodes fabricated by conventional slurry-casting processes. Here, Fe–$FeCl_2$–CR electrodes are fabricated using the chemically stable binder polytetrafluoroethylene (PTFE). As illustrated in Fig. 1a, after ball milling, nano-Fe and $FeCl_2$ powders are repeatedly calendered with the binder and conductive additive (acetylene black) to produce a freestanding Fe–$FeCl_2$–CR electrode with uniform bulk composition.[24] To enhance electronic conductivity in three-electrode tests and large-area cells, a molybdenum mesh (75 μm aperture) is calendered into the interior of the Fe–$FeCl_2$–CR electrode to serve as the integrated current collector. Prior to testing, all electrodes are heat-treated at 250 °C under an Ar atmosphere to promote intermolecular cross-linking of the binder and remove residual moisture.[25] Fig. 1b and c reveal different-magnification SEM images of the

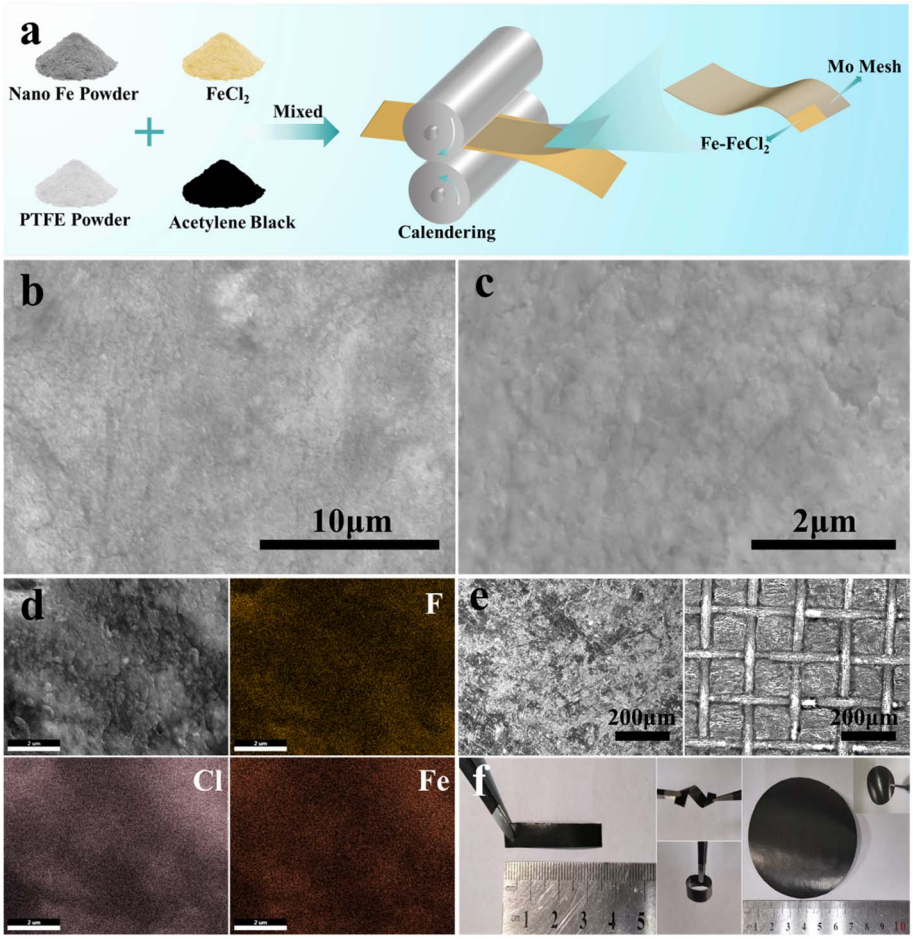

Fig. 1 (a) Preparation diagram of the dry powder calendered Fe/$FeCl_2$–CR electrode. (b and c) SEM images of the Fe/$FeCl_2$–CR electrode surface. (d) SEM-EDS elemental mapping images of the Fe/$FeCl_2$–CR electrode. (e and f) Optical images of both sides of the Fe/$FeCl_2$–CR electrode embedded with molybdenum mesh.

calendered Fe–$FeCl_2$–CR electrode, in which the low-magnification image shows a uniform granular composition without cracks or voids. Fig. 1c further demonstrates that the Fe–$FeCl_2$–CR electrode surface primarily consists of PTFE-encapsulated granular materials, with active substances (nano Fe powder and $FeCl_2$ powder) homogeneously dispersed. Combining the corresponding SEM-EDS images in Fig. 1d, it can be observed that the Fe–$FeCl_2$–CR electrode surface is mainly composed of F (PTFE), Cl ($FeCl_2$), and Fe (Fe or $FeCl_2$) elements, confirming the excellent material uniformity in the Fe–$FeCl_2$–CR electrode prepared by the calendering process. Fig. 1e presents optical images of both sides pf the Fe-$FeCl_2$-CR electrode with molybdenum mesh embedding. Owing to the excellent ductility and adhesion ability of PTFE, the Fe–$FeCl_2$–CR electrode in the three-electrode system embedded with molybdenum mesh exhibits superior mechanical strength and toughness. 360° bending and twisting in Fig. 1f further confirm the excellent flexibility and mechanical strength of the Fe–$FeCl_2$–CR electrode. The preparation of the Fe–$FeCl_2$–CR electrode with expanded area (11.3 cm^2) demonstrates the feasibility of this dry powder process strategy in large-scale practical applications.

The Fe/$FeCl_2$–graphite molten salt battery operates in the $AlCl_3$/LiCl/NaCl ternary inorganic molten salt electrolyte. As shown in Fig. 2a, during charging, the $FeCl_2$ negative electrode is reduced to metallic Fe^0 and NaCl, while the graphite positive electrode undergoes intercalation of AlCl-4 anions into its layers, forming the corresponding graphite intercalation compounds. The discharge process corresponds to the reverse reactions.[12,15] In practice, the battery is assembled in the fully discharged state, with $FeCl_2$ and pristine graphite paper serving as the active materials for the negative and positive electrodes, respectively. To examine the material properties of the dry powder calendered $FeCl_2$–CR electrode, Fig. 2b and c present its XRD pattern and Raman spectrum. The XRD pattern shows clear diffraction peaks corresponding to crystalline $FeCl_2$ (PDF#01-1106) and PTFE (PDF#47-2217). In the Raman spectrum, the peaks at 1353 cm^{-1} and 1597 cm^{-1} originate from the D and G bands of sp^2-hybridized carbon in the acetylene black, while the peak at 229 cm^{-1} is characteristic of $FeCl_2$ in the electrode.

To compare the electronic conductivity of $FeCl_2$ and its reduction product (Fe^0), DC pulse-resistance measurements (pulse duration: 0.5 s) were performed on an Al–$FeCl_2$ half-cell

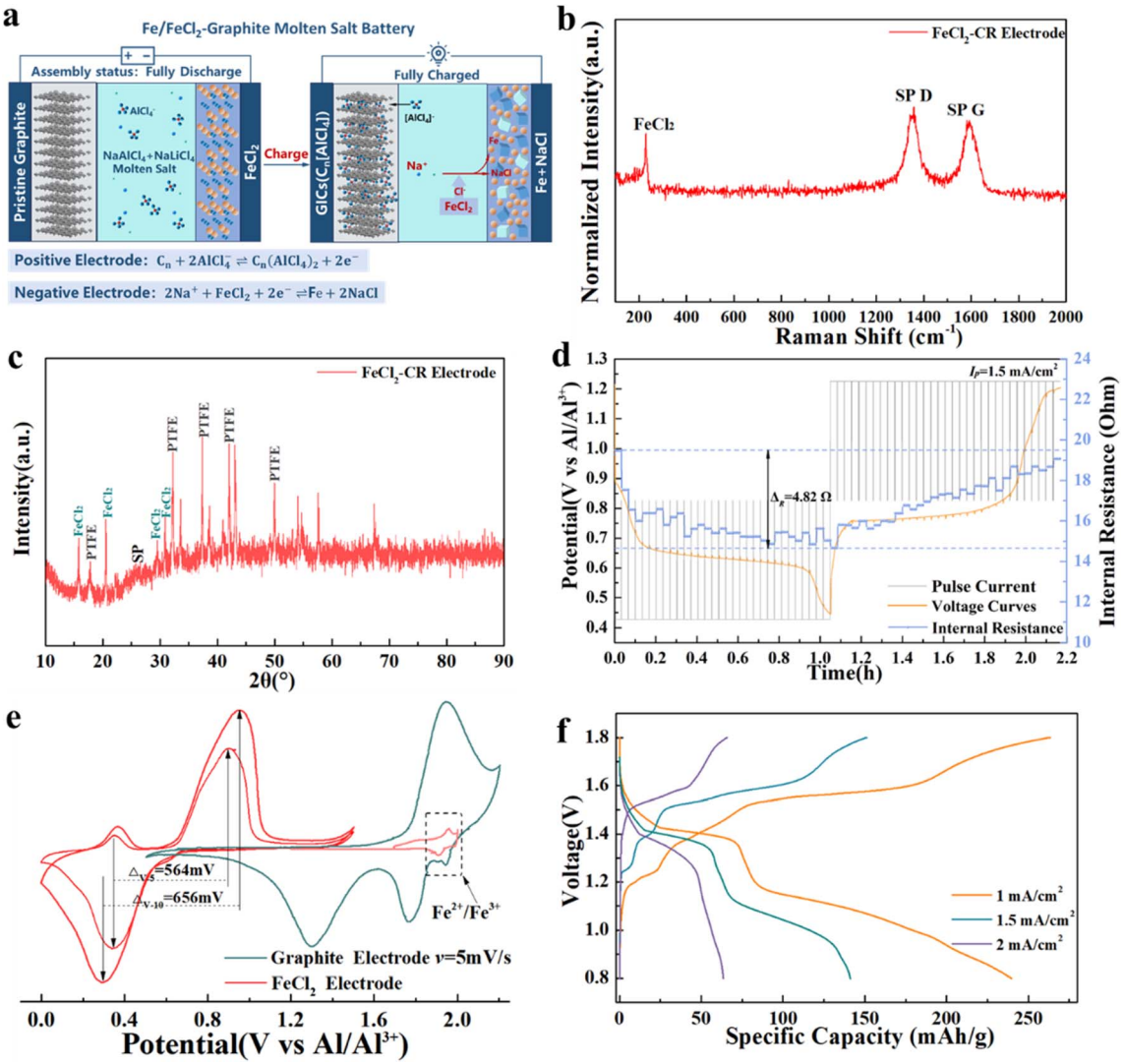

Fig. 2 (a) Preparation diagram of the Fe/$FeCl_2$–graphite molten salt battery. (b) Raman spectrum of the $FeCl_2$–CR electrode. (c) XRD pattern of the $FeCl_2$–CR electrode. (d) DC pulse resistance measurements of the $FeCl_2$–CR electrode in the Al–$FeCl_2$ half-cell during charge/discharge. (e) Cyclic voltammetry curves of the $FeCl_2$–CR electrode and graphite electrode at different scan rates in a three-electrode system. (f) Voltage profiles of the Fe/$FeCl_2$–graphite molten salt battery at various current densities.

to monitor the internal resistance changes during reduction and oxidation. As shown in Fig. 2d, the internal resistance decreases from 19.48 Ω ($FeCl_2$ phase) to 14.66 Ω (Fe + NaCl phase) during discharge, corresponding to the resistance drop of $\Delta R = 4.82$ Ω, which is primarily attributed to the higher electronic conductivity of metallic Fe compared to $FeCl_2$. To investigate the electrochemical window of the molten salt electrolyte, we performed CV tests by using metallic gold (Au) as the working electrode. As shown in Fig. S2, the Au electrode exhibited two extreme electrochemical reactions at a scan rate of 10 mV s^{-1}, corresponding to the evolution of chlorine gas and the deposition/dissolution reaction of metallic aluminum at 2.2 V and −0.04 V, respectively. This is close to the electrochemical window of similar molten salt electrolytes ($AlCl_3$/NaCl) (approximately 0–2.2 V, *vs.* Al/Al^{3+}).[26,27] To explore the electrochemical behavior of the pure $FeCl_2$ electrode and graphite paper electrode, cyclic voltammetry was carried out in a three-electrode configuration using metallic aluminum as both the reference and counter electrode, within the potential window of 0–2.2 V (test setup shown in Fig. S1). When the scan rate is increased from 5 to 10 mV s^{-1}, the $FeCl_2$–CR electrode displayed reduction and oxidation peaks near 0.3 V and 0.9 V, corresponding to the Fe^{2+}/Fe^0 redox couple, consistent with the reported electrode potentials of $FeCl_2$ in ionic-liquid electrolytes.[16]

In the $AlCl_3$–NaCl–LiCl electrolyte, the redox behavior of the $FeCl_2$–CR electrode (Fe^{2+}/Fe^0) and the graphite electrode (C_n/C_n[-AlCl-4]) was further characterized within the potential range of 1.2–2.0 V. The results show that the oxidation and reduction reactions of $FeCl_2$ proceed within the potential window of AlCl-4 intercalation/deintercalation into graphite, confirming the absence of significant high-potential side reactions at the $FeCl_2$–

CR electrode during the operation of the Fe/$FeCl_2$–graphite full cell. The peak separation (in Fig. 2e) between oxidation and reduction potentials increases from 564 mV to 656 mV as the scan rate increases, indicating sluggish reaction kinetics inherent to the bulk $FeCl_2$ material. The voltage profiles and cycling performance of the $FeCl_2$–CR electrode in the full-cell configuration are presented in Fig. 2f and S4. The electrode delivers discharge specific capacities of 239.7, 141.2, and 63.5 mAh g^{-1} at current densities of 1, 1.5, and 2 mA cm^{-2}, respectively. The poor capacity retention at higher current densities is likely due to high nucleation energy barriers and significant internal resistance differences. Furthermore, the distinct charge/discharge plateaus nearly vanish at 2 mA cm^{-2} upon cycling, suggesting that metallic Fe^0 formed from the reduction of pure $FeCl_2$ cannot be fully re-oxidized in the subsequent charging step, leading to limited reversibility.

Based on the electrochemical behavior of the pure $FeCl_2$–CR electrode and prior observations, the lack of a compatible Fe^0 nucleation interface on pristine $FeCl_2$ is likely the main reason for its poor reversibility and sluggish kinetics. As illustrated in Fig. 3a and b, the high nucleation energy barrier and lattice mismatch of bulk $FeCl_2$ can cause the reduction product (Fe^0) to aggregate into clusters, resulting in a discontinuous and inefficient active interface. To provide compatible nucleation sites for Fe^0 and lower the interfacial energy barrier, we introduced nano-Fe powder as a pre-formed Fe interface to construct a continuous and stable reduction interface. As shown in Fig. S5–S10, the cycling performance of Fe–$FeCl_2$–CR electrodes with different nano-Fe contents was evaluated in the full-cell configuration. The Fe–$FeCl_2$–CR-60 electrode (with 60 wt% nano-Fe) exhibited the best capacity retention and electrochemical stability. A comprehensive analysis (Fig. S11) reveals that this electrode achieves the highest active-material utilization (27.15%) and an average specific capacity of 172.28 mAh g^{-1}, along with the smallest capacity fluctuation (−0.04 mAh g per cycle) over 100 cycles.

Notably, electrodes with nano-Fe contents below 60 wt% show gradual capacity decay during cycling, whereas those with nano-Fe above 60 wt% display a capacity increase, which may be attributed to the initial activation of the nano-Fe interface. Similar activation behavior, involving the displacement of the subsurface passivation layer on nano-Fe, has been reported in Na–$NiCl_2$ molten-salt batteries.[28,29] Therefore, we systematically investigated the electrochemical properties of the optimized Fe–$FeCl_2$–CR-60 electrode in both three-electrode and Al–$FeCl_2$ half-cell setups. Fig. 3c and S3 present the CV curves at different scan rates (5 mV s^{-1}, 10 mV s^{-1}, 15 mV s^{-1} and 20 mV s^{-1}) of the Fe–$FeCl_2$–CR-60 electrode under the same conditions. The oxidation/reduction polarization potentials of the electrode at the corresponding scan rates are 381 mV, 425 mV, 486 mV, and 549 mV, indicating that the oxidation/reduction reaction kinetics based on the Fe interface still need further improvement. Additionally, the CV curves exhibit stable oxidation/reduction current peaks at different scan rates, demonstrating that the electrochemical reaction in the Fe–$FeCl_2$–CR-60 electrode possesses excellent electrode reversibility. Compared to the pure $FeCl_2$–CR electrode (in Fig. 2e), the pre-addition of nano-Fe reduces the polarization of the $FeCl_2$ bulk by 24.82% and 23.02% at these scan rates. The resulting Fe/Fe^{2+} redox potentials (0.4–0.5 V for reduction and 1.0–1.1 V for oxidation *vs.* Al/Al^{3+}) align well with those reported for the iron metal electrode in the Na–$FeCl_2$ molten-salt battery ($NaAlCl_4$ electrolyte at 190 °C).[30] In the Al–Fe/$FeCl_2$ half-cell, the voltage profiles of the Fe–$FeCl_2$–CR-60 electrode (Fig. 3d) show clear charge and discharge plateaus at 0.74 V and 0.65 V, respectively, corresponding to a galvanostatic polarization voltage of only 90 mV. DC pulse-resistance measurements (Fig. 3e) further reveal that the overall DC resistance of this electrode ranges from 10.21 to 11.95 Ω. The resistance difference between the oxidized and reduced states is reduced by 69.58% compared to the pure $FeCl_2$–CR electrode, primarily due to the continuous conductive network provided by the nano-Fe particles. Fig. 3f presents the stable voltage profile of the optimized Fe–$FeCl_2$–CR-60 negative electrode during long-term cycling in the full-cell configuration. At a current density of 3.0 mA cm^{-2}, the electrode delivers a specific capacity of 163.89 mAh g^{-1} after 200 cycles, significantly higher than the 28.81 mAh g^{-1} obtained with the pure $FeCl_2$–CR negative electrode. Fig. S6 further confirms the electrochemical reversibility of the Fe–$FeCl_2$–CR-60 electrode at moderate active mass loading (Fe + $FeCl_2$: 7.57 mg cm^{-2}); the specific capacity of the Fe–$FeCl_2$–CR-60 electrode is 114.62 mAh g^{-1} after 200 cycles. In current research on metal chloride electrodes, similar cycling stability performance is acceptable. For example, Li *et al.* developed a low-cost Na–$FeCl_2$ battery system based on the Fe/Fe^{2+} redox reaction under operating conditions of 190 °C. By adding a small amount of metallic nickel powder (10 mol%), the corresponding Fe/Ni/NaCl electrode achieved an energy density of 295 Wh kg^{-1} after 200 cycles ($\approx C/5$).[30] Under the same operating temperature conditions, Wen *et al.* developed a three-dimensional active Ni/NaCl electrode in the Na–$NiCl_2$ battery by using Ni–carbon composite nanofiber as the matrix material. The continuous three-dimensional conductive network derived from electrospun fibers effectively limits the growth of grains. And the NCCN-based electrode shows almost no capacity degradation after 350 cycles at 2C.[31]

Building on the optimized reduction interface achieved by pre-adding nano-Fe to the $FeCl_2$ bulk, we conducted a comprehensive evaluation of the Fe–$FeCl_2$–CR-60 electrode within the full Fe/$FeCl_2$–graphite molten salt battery. As shown in Fig. 4a and b, the electrode delivers specific capacities of 190.84, 187.55, 161.16, 140.13, 123.79, and 114.33 mAh g^{-1} at current densities of 2.5, 3, 4, 5, 6, and 7 mA cm^{-2}, respectively. When the current density is returned to 2.5 mA cm^{-2}, the specific capacity recovers to 215.18 mAh g^{-1}, demonstrating excellent rate capability and fast reaction kinetics. Owing to the insulating nature of molten-salt electrolytes at room temperature, the application fields of these molten salt batteries mainly include thermoelectric combined scenarios, such as low-grade waste heat utilization and molten salt thermal storage power stations, where they are suitable for long-term freeze-thaw reserve batteries and grid-level seasonal storage by virtue of the solidification and insulating characteristics of molten salt electrolytes. Li *et al.* systematically demonstrated the application feasibility of molten salt batteries for seasonal energy

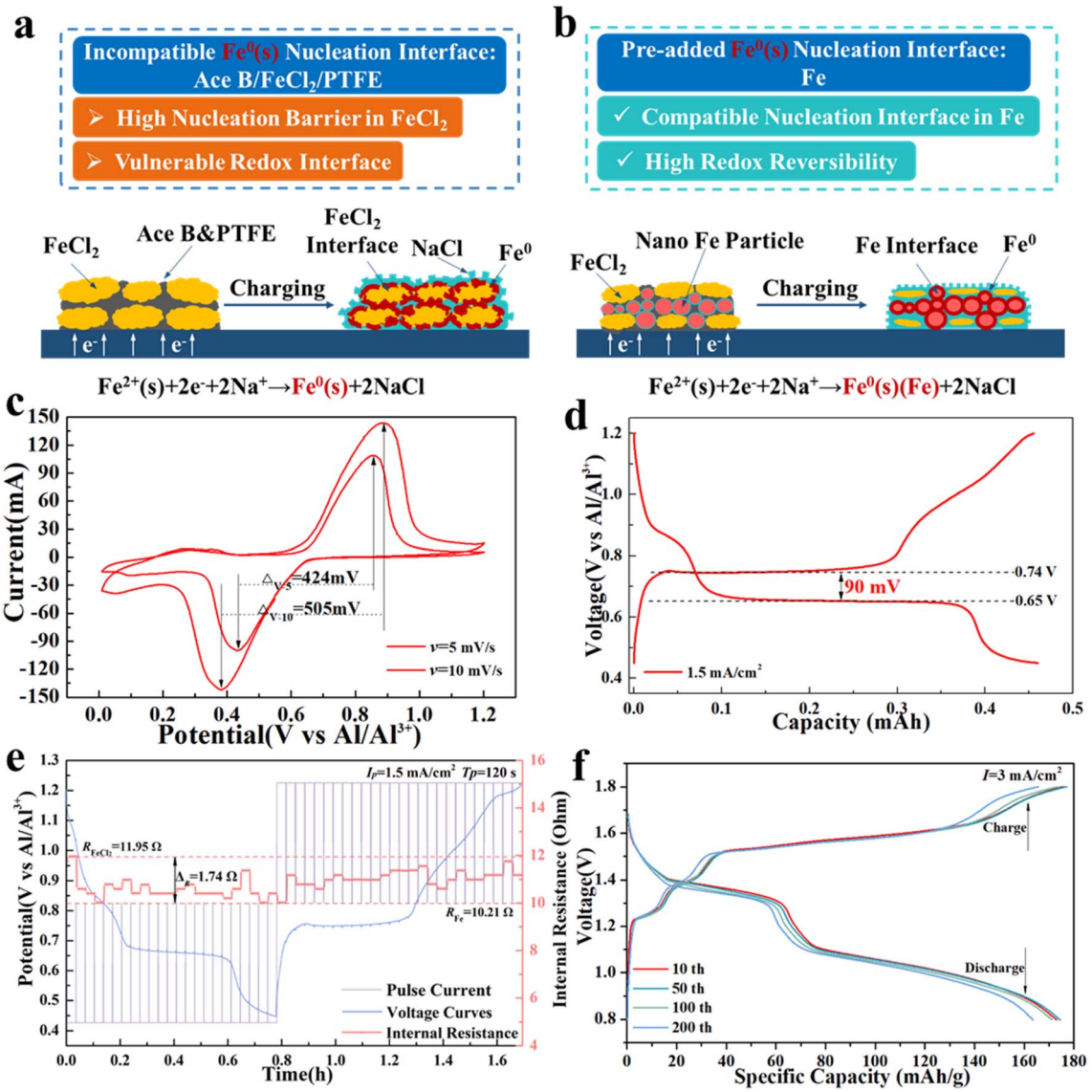

Fig. 3 (a and b) Schematic illustration of the interface reduction mechanism at the $FeCl_2$–CR electrode and the Fe–$FeCl_2$–CR electrode. (c) Cyclic voltammetry curves of the Fe–$FeCl_2$–CR electrode at varied scan rates. (d) Charge/discharge profiles of the Fe–$FeCl_2$–CR electrode in the Al–Fe/$FeCl_2$ half-cell. (e) DC pulse resistance testing of the Fe–$FeCl_2$–CR electrode. (f) Cycling performance of the Fe–$FeCl_2$–CR electrode in Fe/$FeCl_2$–graphite molten salt batteries.

storage in Al–Ni molten salt battery systems, achieving an effective capacity recovery of over 90% after 1–8 weeks of storage as a valid proof-of-concept.[32] Therefore, to assess their feasibility for room-temperature reserve applications, a fully charged Fe/$FeCl_2$–graphite battery is cooled under natural conditions (Fig. 4c) and rested at room temperature for one week before being discharged after temperature restoration. The results show nearly identical discharge voltage plateaus and a retained specific capacity of 196.7 mAh g^{-1}, indicating excellent reserve characteristics and low self-discharge. Furthermore, to verify the electrochemical performance reliability of the Fe–$FeCl_2$–CR-60 electrode prepared by the dry powder calendering process, we extended the capacity of the Fe/$FeCl_2$–graphite test battery to greater than 10 mAh by simply expanding the electrode reaction area to 11.3 cm^2 (in Fig. 4d). As shown in Fig. 4e and f, an initial capacity of 13 mAh was obtained with an electrode area of 11.3 cm^2, and a discharge capacity of 11.1 mAh was maintained after 18 cycles at a current of 6 mA, indicating that the Fe–$FeCl_2$–CR-60 electrode with an expanded active area still exhibits reversible electrode reactions. The charge/discharge plateaus at approximately 1.5 V and 1.4 V/1.2 V (Fig. 4f) are consistent with the electrochemical behavior observed in small-scale test cells (Fig. 4b). This provides a feasible route for increasing the single cell capacity in the future.

To investigate the electrochemical activity of the nano-Fe interface in the oxidation reaction, we further examined the reversibility of an electrochemical pre-oxidized nano-Fe electrode in the Fe/$FeCl_2$–graphite molten salt battery. In the electrochemical oxidation reaction, the Fe-CR-100 electrode and aluminum metal are used as the oxidizing anode and cathode,

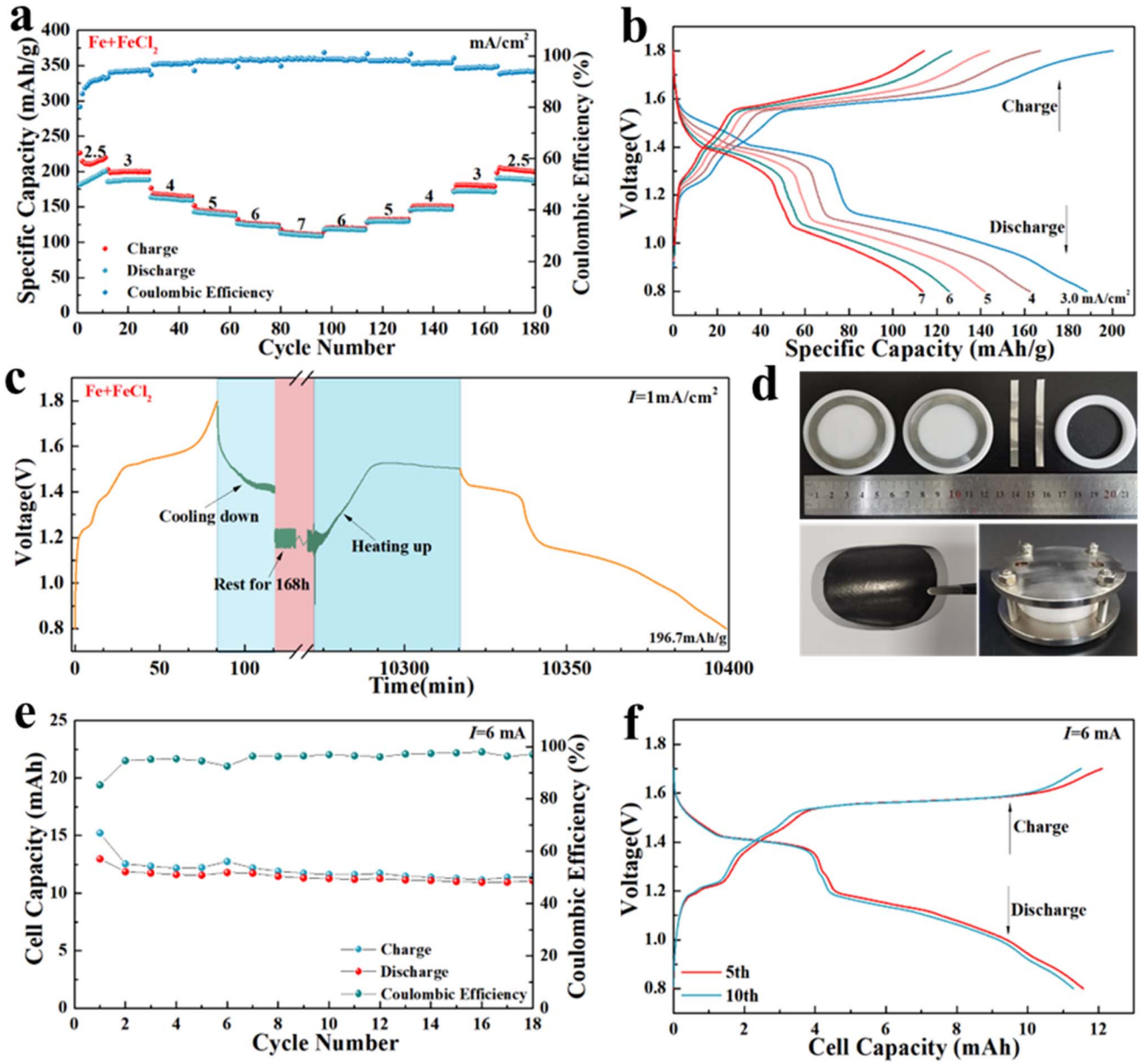

Fig. 4 (a) Rate performance of the Fe–$FeCl_2$–CR-60 electrode in Fe/$FeCl_2$–graphite molten salt batteries. (b) Corresponding voltage profiles at varied current densities. (c) Cooling storage characteristics of the Fe/$FeCl_2$–graphite molten salt battery. (d) Assembly images of the Fe/$FeCl_2$–graphite molten salt battery with a capacity expanded Fe–$FeCl_2$–CR-60 negative electrode. (e and f) Cycling profile and voltage curves of the capacity expanded Fe/$FeCl_2$–graphite molten salt battery.

respectively. As shown in Fig. 5a, the initial interface oxidation is performed in the Al–Fe half-cell by galvanostatic anodic polarization at 1 mA cm^{-2} (potential curve in Fig. S12). During this galvanostatic anodic process, the nano-Fe surface undergoes Fe → Fe^{2+} oxidation, forming $FeCl_2$ and a solid oxide film containing Fe^{2+}.[15] The Fe/$FeCl_2$–graphite battery is then reassembled by using the electrochemical oxidized Fe-CR-100 electrode. The performance is shown in Fig. 5b and c. The oxidized negative electrode delivers an initial capacity of 163.63 mAh g^{-1} at 1 mA cm^{-2}. When the current density is increased to 2 mA cm^{-2}, a specific capacity of 136.98 mAh g^{-1} is maintained, confirming that the Fe^{2+} formed during pre-oxidation can be reversibly reduced upon charging and that the nano-Fe particle interface is gradually activated as the dominant electroactive interface. The corresponding voltage curves (Fig. 5c) show charge plateaus at ~1.33 V, 1.39 V and 1.54 V, and discharge plateaus at ~1.41 V and 1.12 V, which are nearly identical to those of the Fe–$FeCl_2$–CR-60 electrode (Fig. 4b). This indicates that the $FeCl_2$ formed on the nano-Fe surface after pre-oxidation is reduced during the first charge, and the activated nano-Fe interface thereafter exhibits the same electrochemical behavior as that in the Fe–$FeCl_2$–CR-60 electrode. After 200 cycles, the electrode retains a specific capacity of 93.78 mAh g^{-1}, demonstrating that redox reactions occurring at the pure nano-

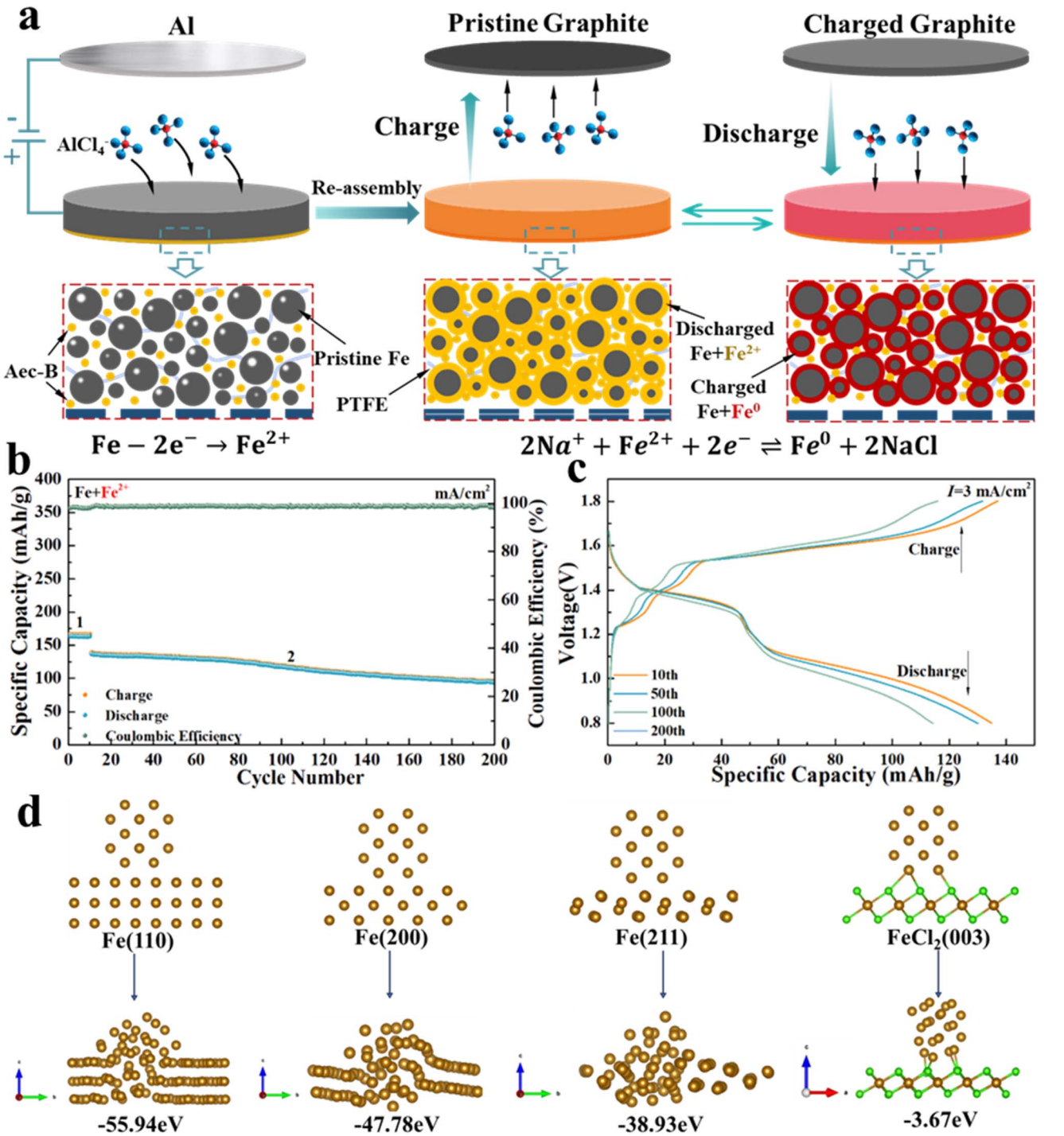

Fig. 5 (a) Schematic of the electrochemical activation process of the 100 wt% nano-Fe powder electrode (Fe–CR-100) and electrode reaction mechanism in the reassembled full cell. (b and c) Cycling performance and voltage curves of the activated Fe–CR-100 electrode in Fe/$FeCl_2$–graphite molten salt batteries. (d) DFT calculation of iron cluster atoms on different material crystal planes.

Fe interface possess superior reversibility compared to the pure $FeCl_2$ electrode ($FeCl_2$–CR, Fig. S4). This finding is consistent with our previous research, in which the Fe^{2+}-containing oxide film can form on the metallic Fe foam surface under oxidative conditions, and the interfacial oxidized Fe^{2+} film exhibits excellent electrochemical reversibility in the Fe/$FeCl_2$–graphite molten salt battery (the Fe/Fe^{2+} negative electrode prepared by an electrochemical anodic electrolysis strategy, exhibits a stabilized capacity of 0.72 mAh cm^{-2} after 7000 cycles at 5 mA cm^{-2}, with a low polarization level of about 29 mV).[15] By simulating the oxidation atmosphere during electrode discharging, similar oxidation behavior was observed for the nano-Fe electrode.

Therefore, the excellent reversibility and rate capability of the optimized Fe–$FeCl_2$–CR-60 electrode are primarily attributed to the initial $FeCl_2$ supply and the progressive activation of the nano-Fe particle interface, which gradually becomes the dominant region governing electrode capacity and electrochemical activity.

To understand the difference in nucleation stability of metallic Fe^0 generated from the reduction of initial $FeCl_2$, DFT calculations are performed to compare the binding energies of Fe^0 atomic clusters on different $FeCl_2$ and Fe crystal planes according to the main crystal planes detectable in XRD testing (as shown in Fig. S13 and S14). As illustrated in Fig. 5d, the binding energy (the detailed information is shown in Fig. S15–S18) between Fe^0 clusters and the main crystal planes of nano-Fe powder is higher than that of the surface of $FeCl_2$ under the same conditions. That is to say, compared to the $FeCl_2$ material in the Fe–$FeCl_2$–CR electrode, the crystal surfaces (110, 200 and 211) of nano-Fe powder are more likely to become the main nucleation interfaces for Fe^0 clusters. In summary, the nano-Fe powder in the Fe–$FeCl_2$–CR-60 electrode provides an Fe-philic nucleation interface for reduced Fe^0, while $FeCl_2$ serves as the initial oxidized active material to meet the assembly requirement of the fully discharged Fe/$FeCl_2$–graphite battery.

To elucidate the reaction mechanism of the dry-powder-calendered $FeCl_2$ electrode during charging, the reaction products and interfacial changes in the fully charged Fe/$FeCl_2$–graphite molten salt battery are analyzed. As shown in Fig. 6a–f, compared with the pristine surface of the calendered electrode, the charged $FeCl_2$ electrode shows uniform granular products (average particle size ~0.22 μm) adhering to the outer layer. SEM-EDS analysis reveals that these granules are primarily composed of Cl and Na, confirming that the charging process involves the formation of a NaCl solid phase. The Fe signal on the electrode surface is relatively low, likely because the electrolyte-derived membrane (containing Al and O) covers the underlying Fe^0 product. According to the Raman spectra in Fig. 6g, the peaks at 1357 cm^{-1} and 1591 cm^{-1} in the pristine $FeCl_2$ electrode correspond to the D and G bands of the conductive agent acetylene black, while the signal at 229 cm^{-1} is assigned to $FeCl_2$. In contrast to the characteristic peaks of acetylene black, the peak near 229 cm^{-1} disappears in the fully charged electrode, mainly because $FeCl_2$ is almost completely reduced to metallic Fe^0 during charging. Metallic elements do not exhibit Raman signals due to the absence of molecular vibrations. The XRD pattern in Fig. 6h further confirms the phase transformation of the $FeCl_2$ electrode upon charging. The diffraction peaks at 58.81° and 73.62° are attributed to the molybdenum mesh current collector. Peaks at 27.29°, 31.75°, 45.51°, and 56.60° correspond to the (111), (200), (220), and (222) crystal planes of NaCl, respectively. The crystallization of NaCl particles on the electrode surface indicates that the electrolyte accessible $FeCl_2$ undergoes reduction during the charging process.

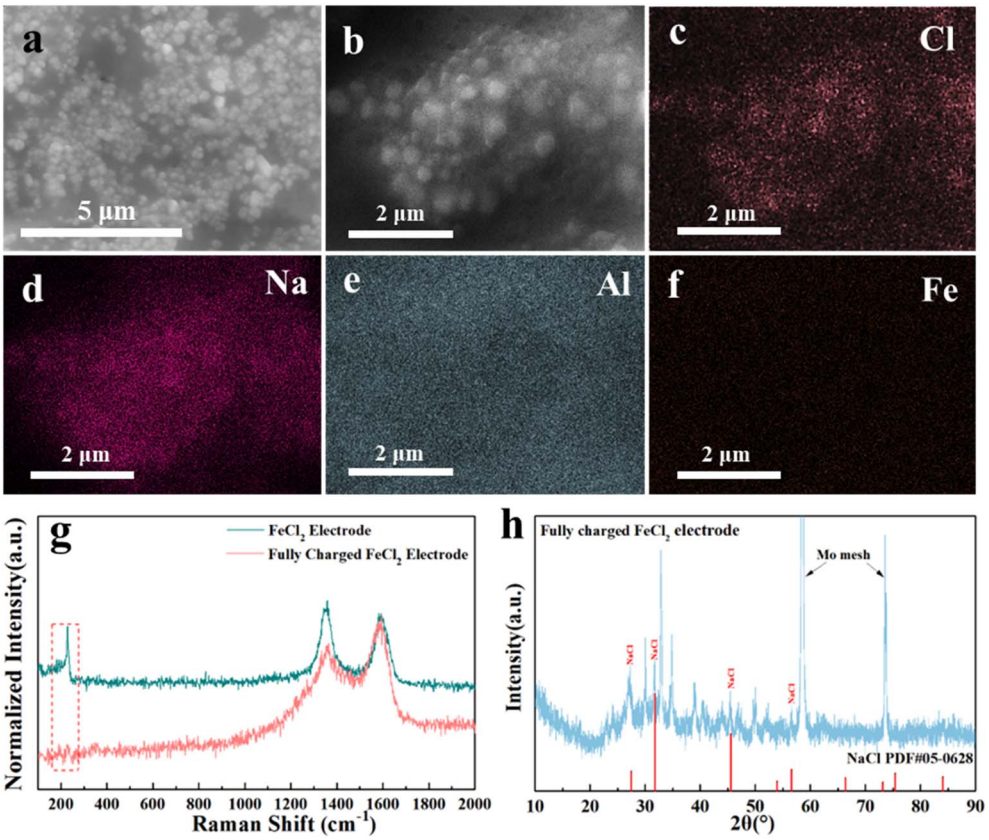

Fig. 6 (a and b) SEM images of the fully charged pure $FeCl_2$–CR electrode. (c–f) SEM-EDS elemental mapping of the pure $FeCl_2$–CR electrode. (g) Raman spectra of the pristine and the fully-charged $FeCl_2$–CR electrodes. (h) XRD pattern of the fully-charged $FeCl_2$–CR electrode.

4. Conclusions

In summary, the Fe–$FeCl_2$ contact interface is constructed for the Fe/$FeCl_2$ negative electrode *via* a solvent-free powder-calendering strategy. Here, nano-Fe powder mainly serves as a potential Fe-philic nucleation interface to induce the distribution of reduced Fe^0, while $FeCl_2$ acts as the initial oxidation agent to meet the assembly requirement of the battery in a fully discharged state. Unlike the pure interfacial oxidation (Fe → Fe^{2+}) in chemical or electrochemical chlorination, the repeated dry-powder-calendering process provides sufficient contact between metallic Fe and $FeCl_2$, which favors the nucleation and growth of reduced Fe^0 on the nano-Fe interface. The Fe–$FeCl_2$–CR-60 electrode exhibits low redox overpotential (0.09 V) and DC pulse internal resistance (1.74 Ω) compared with the $FeCl_2$–CR electrode. In the Fe/$FeCl_2$–graphite molten salt battery, the Fe–$FeCl_2$–CR-60 electrode delivers a specific capacity of 162.6 mAh g^{-1} at 3 mA cm^{-2} and retains 93% of its capacity after 200 cycles, with the active-material utilization increasing to 27.15%. DFT calculations reveal that the Fe (110) crystal plane in the Fe–$FeCl_2$ hetero-interface possesses the highest binding energy (−55.94 eV), which facilitates the nucleation and growth of reduced Fe^0 clusters. Pre-oxidation experiments on the Fe–CR-100 electrode suggest that the surface of nano-Fe powder can be activated during electrochemical oxidation, thereby improving the electrode's electrochemical reversibility and ultimately leading to a stable, reversible electrochemical interface. Corresponding room-temperature self-discharge tests and capacity-expanded experiments further confirm the electrochemical reaction stability of the calendered Fe–$FeCl_2$–CR electrode for Fe/$FeCl_2$–graphite molten salt batteries.

Author contributions

Wenlong Zhang: conceptualization, data curation, formal analysis, visualization funding acquisition, writing – original draft. Xiaohui Ning: project administration, resources, funding acquisition, supervision, validation, writing – review and editing.

Conflicts of interest

There are no conflicts to declare.

Data availability

The authors declare that the data supporting the findings of this study are available within the paper and its supplementary information (SI) files. Should any raw data files be needed in another format they are available from the corresponding author upon reasonable request. Source data are provided with this paper. Supplementary information is available. See DOI: https://doi.org/10.1039/d6sc03818b.

Acknowledgements

This work was supported by the National Natural Science Foundation of China (52504339, 92372205, and 51874228) and the Natural Science Foundation of Shaanxi Province, China (2020JM-068). The author gratefully acknowledges the support of the K. C. Wong Education Foundation.

References

1 C. Chen, C.-S. Lee and Y. Tang, *Nano-Micro Lett.*, 2023, **15**, 121.
2 Q. Pang, J. Meng, S. Gupta, X. Hong, C. Y. Kwok, J. Zhao, Y. Jin, L. Xu, O. Karahan, Z. Wang, S. Toll, L. Mai, L. F. Nazar, M. Balasubramanian, B. Narayanan and D. R. Sadoway, *Nature*, 2022, **608**, 704–711.
3 L. Wang, Q. Li, Y. Wang, Y. Li, Z. Chen, L. Jiang and B. Tang, *Energy*, 2024, **309**, 133140.
4 Y. Li, Y. Wang, Z. Chen, Q. Li, J. Du, J. Chai, L. Wang, Y. Rui, L. Jiang and B. Tang, *Chem. Eng. J.*, 2023, **476**, 146577.
5 Y. Wang, Y. Li, J. Chai, Q. Li, J. Du, Y. Rui, B. Tang and L. Jiang, *Chem. Eng. J.*, 2024, **481**, 148485.
6 L. Jiang, F. Liang, Z. Zhang, D. Wu, J. Chai, T. Luo, N. Han, W. Zhang, Y. Rui and B. Tang, *Chem. Eng. J.*, 2022, **433**, 133568.
7 X. Ning, S. Phadke, B. Chung, H. Yin, P. Burke and D. R. Sadoway, *J. Power Sources*, 2015, **275**, 370–376.
8 H. Wang and C. Peng, *Sustain. Energy Fuels*, 2023, **7**, 330–354.
9 S. J. Percival, A. M. Maraschky, M. L. Meyerson, M. A. Stalcup, A. S. Peretti, L. J. Small and E. D. Spoerke, *Ind. Eng. Chem. Res.*, 2025, **64**, 22714–22723.
10 M.-C. Lin, M. Gong, B. Lu, Y. Wu, D.-Y. Wang, M. Guan, M. Angell, C. Chen, J. Yang, B.-J. Hwang and H. Dai, *Nature*, 2015, **520**, 324–328.
11 J. Tu, J. Wang, H. Zhu and S. Jiao, *J. Alloys Compd.*, 2020, **821**, 153285.
12 T. Dai, L. Yang, X. Ning, D. Zhang, R. L. Narayan, J. Li and Z. Shan, *Energy Storage Mater.*, 2020, **25**, 801–810.
13 G. Li, X. Lu, J. Y. Kim, V. V. Viswanathan, K. D. Meinhardt, M. H. Engelhard and V. L. Sprenkle, *Adv. Energy Mater.*, 2015, **5**, 1500357.
14 G. Feng, Z. Liu, J. Holoubek, L. C. Greenburg, G. Zhang, Y. Li, X. Guan, Y. Cui, P. Zhang, A. Brest, X. Zheng and Y. Cui, *Nat. Commun.*, 2025, **16**, 11055.
15 W. Zhang, H. Li and X. Ning, *ACS Appl. Mater. Interfaces*, 2024, **16**, 30545–30555.
16 H. Yang, F. Wu, W. Liu, X. Wang, Y. Bai and C. Wu, *Energy Storage Mater.*, 2022, **51**, 435–442.
17 W. Zhang, H. Li, H. Zhou and X. Ning, *J. Power Sources*, 2024, **593**, 233958.
18 G. Kresse and J. Furthmüller, *Comput. Mater. Sci.*, 1996, **6**, 15–50.
19 G. Kresse and J. Furthmüller, *Phys. Rev. B: Condens. Matter Mater. Phys.*, 1996, **54**, 11169–11186.
20 J. P. Perdew, K. Burke and M. Ernzerhof, *Phys. Rev. Lett.*, 1996, **77**, 3865–3868.

21 G. Kresse and D. Joubert, *Phys. Rev. B: Condens. Matter Mater. Phys.*, 1999, **59**, 1758–1775.
22 P. E. Blöchl, *Phys. Rev. B: Condens. Matter Mater. Phys.*, 1994, **50**, 17953–17979.
23 S. Grimme, J. Antony, S. Ehrlich and H. Krieg, *J. Chem. Phys.*, 2010, **132**, 154104.
24 J. Hong, J. Yoon, J.-W. Park, Y.-C. Ha, J. Lee and I. Hwang, *J. Power Sources*, 2025, **655**, 237925.
25 B. G. Meyer, G. Matthews, R. Scales, N. C. Mitchell, E. Darnbrough, R. A. House, D. E. J. Armstrong and P. S. Grant, *ACS Mater. Lett.*, 2025, **7**, 3444–3451.
26 Y. Song, S. Jiao, J. Tu, J. Wang, Y. Liu, H. Jiao, X. Mao, Z. Guo and D. J. Fray, *J. Mater. Chem. A*, 2017, **5**, 1282–1291.
27 J. Tu, W.-L. Song, H. Lei, Z. Yu, L.-L. Chen, M. Wang and S. Jiao, *Chem. Rev.*, 2021, **121**, 4903–4961.
28 X. Ao, Z. Wen, Y. Hu, T. Wu, X. Wu and Q. He, *J. Power Sources*, 2017, **340**, 411–418.
29 G. Li, X. Lu, J. Y. Kim, M. H. Engelhard, J. P. Lemmon and V. L. Sprenkle, *J. Power Sources*, 2014, **272**, 398–403.
30 X. Zhan, M. E. Bowden, X. Lu, J. F. Bonnett, T. Lemmon, D. M. Reed, V. L. Sprenkle and G. Li, *Adv. Energy Mater.*, 2020, **10**, 1903472.
31 X. Gao, Y. Hu, Y. Li, J. Wang, X. Wu, J. Yang and Z. Wen, *ACS Appl. Mater. Interfaces*, 2020, **12**(22), 24767–24776.
32 M. M. Li, X. Zhan, E. Polikarpov, N. L. Canfield, M. H. Engelhard, J. M. Weller, M. D. Reed, V. L. Sprenkle and G. Li, *Cell Rep. Phys. Sci.*, 2022, **3**(4), 100821.